Highly Efficient Performance and Conversion Pathway of Photocatalytic NO Oxidation on SrO@Amorphous Carbon Nitride

Wen Cui [a], *Jieyuan Li* [b], *Fan Dong* [a,*], *Yanjuan Sun* [a], *Guangming Jiang* [a], *Wanglai Cen* [b], *S. C. Lee* [c], *Zhongbiao Wu* [d]

[a] Chongqing Key Laboratory of Catalysis and New Environmental Materials, College of Environment and Resources, Chongqing Technology and Business University, Chongqing 400067, China.

[b] College of Architecture and Environment, Institute of New Energy and Low Carbon Technology, Sichuan University, Sichuan 610065, China.

[c] Department of Civil and Environmental Engineering, The Hong Kong Polytechnic University, Hong Kong, China.

[d] Department of Environmental Engineering, Zhejiang University, Hangzhou 310027, China.

* To whom correspondence should be addressed. E-mail: dfctbu@126.com (Fan Dong). Phone: +86 23 62769785 605. Fax:+86 23 62769785 605.

ABSTRACT: This work demonstrates a first molecular-level conversion pathway of NO oxidation over a novel SrO clusters@amorphous carbon nitride (SCO-ACN) photocatalyst, which is synthesized via co-pyrolysis of urea and $SrCO_3$. The inclusion of $SrCO_3$ is crucial in the formation of the amorphous carbon nitride (ACN) and SrO clusters by attacking the intralayer hydrogen bonds at edge sites of graphitic carbon nitride (CN). The amorphous property of ACN could promote the transportation, migration and transformation of charge carriers on SCO-CAN. The SrO clusters were identified as the newly formed active centers to facilitate the activation of NO via the formation of Sr-$NO^{\delta(+)}$, which essentially promoted the conversion of NO to final products. The combined effects of amorphous structure and SrO clusters render the SCO-CAN an outstanding photocatalytic NO removal efficiency under visible light illumination. To reveal the photocatalytic mechanism, the adsorption and photocatalytic oxidation processes of NO over CN and SCO-ACN were analyzed *by in situ* DRIFTS, and the intermediates and conversion pathways were elucidated and compared. This work presents a novel *in situ* DRIFTS-based strategy to explore photocatalytic reaction pathway of NO oxidation, which is quite beneficial to understand the mechanism of photocatalytic reaction and advance the development of photocatalytic technology for environmental remediation.

1. INTRODUCTION

Along with the improvement in human life and the growing environmental awareness of people, air pollution is increasingly emphasized by the academia and the public.[1-3] Nitric oxide (NO), as one of the major contributors to photochemical smog, acid rains, ozone depletion and the causes to respiratory diseases and cardiopulmonary diseases, arouses profound social concerns.[4, 5] Conventionally, physical adsorption, biofiltration, and thermal catalysis methods were employed to remove NO from industrial emissions. However, these methods are not economically feasible for NO removal at parts per billion (ppb) levels.[6, 7] As a green technology, photocatalysis has gained considerable attention in view of its facility and high efficiency for solar energy utilization and environmental remediation.[8-10]

Graphitic carbon nitride (CN), a metal-free layered conjugated semiconductor, was firstly reported as a visible-light photocatalyst by Wang et al.[11] Owing to its appealing electronic band structure, physicochemical stability and earth-abundant nature, CN has become a new research hotspot in the arena of environmental remediation and solar energy conversion.[12-14] However, to improve the photocatalytic efficiency and the adaptability in various application fields, further optimization on CN performance is still desirable, and the developed strategy includes inner architecture modification and surface functionalization (elemental doping, copolymerization, and formation of heterojunctions).[15-19] For inner architecture modification, Kang et al. recently synthesized novel amorphous carbon nitride (ACN) through breaking the in-plane hydrogen bonds between strands of polymeric melon units via post-heat treatment of the partially crystalline CN at a high temperature of 620 ℃ for 2 h.[20, 21] The as-prepared ACN eliminated the high localization of photogenerated charge carriers within each melon strand, decreased the large potential barrier between the layers and across the hydrogen bonds located regions, and facilitated the transfer of charge carriers and broadened the light absorption range, leading to a much superior activity in hydrogen generation in comparison with pristine CN.[20, 21]

The conversion pathway of the pollutant removal over the photocatalyst is one essential part, which is beneficial to understand the underlying reaction mechanism,

evaluate the risky in generation of toxic intermediates and optimize the photocatalyst performance. Till now, though tremendous photocatalysts have been developed for NO photocatalytic oxidation, little attention has been put to exploring conversion route of NO during photocatalytic oxidation process.[5, 10, 19, 22, 23] *In situ* DRIFTS is an effective way for gas-phase reaction analysis that can get a signal once there is an even tiny change in molecular level, and is thus very suitable for the examination about reaction pathway of photocatalytic NO oxidation.[24-29]

Here, a facile method was developed to construct SrO clusters@amorphous carbon nitride (SCO-ACN) via co-pyrolysis of urea and $SrCO_3$, which exhibited substantially enhanced visible-light photocatalytic NO removal efficiency. The high efficiency benefits from the amorphous property of ACN which could promote the transportation, migration and transformation of charge carriers and the available enhanced activation of NO via the formation of Sr-$NO^{\delta(+)}$. To reveal the photocatalytic mechanism, the adsorption and photocatalytic oxidation process of NO over CN and SCO-ACN was analyzed *by in situ* DRIFTS, and the intermediates and conversion pathways were elucidated and compared. Notably, SrO clusters were identified as the newly formed active centers to facilitate the activation of NO, which could effectively promote the conversion of NO to final products. This work presents a novel *in situ* DRIFTS-based strategy to explore photocatalytic reaction pathway of NO oxidation, which is quite beneficial to understand the mechanism of photocatalytic reaction and advance the development of photocatalytic technology for environmental remediation.

2. EXPERIMENTAL AND THEORETICAL SECTION

2.1 Preparation of photocatalysts

All chemicals employed in this study were analytical grade and were used without further treatment. In a typical synthesis procedure, 10 g of urea and a certain amount of $SrCO_3$ were added in an alumina crucible (50 mL) with 20 mL distilled water. The obtained solution was transferred to an oven and dried at 60 ℃. And then the crucible with a cover was calcined at 550 ℃ for 2 h with a heating rate of 15 ℃/min in static air. To investigate the effect of ratios between CN and $SrCO_3$, the content of $SrCO_3$

were controlled at 0.06, 0.1 and 0.18 g, respectively, and the prepared samples were labeled as SCO-ACN-X (X represents the amount of $SrCO_3$). For comparison, an ex-situ mechanical mixture of CN and $SrCO_3$ was also prepared and named as SCO-CN.

2.2 Characterization methods

The crystal phase of prepared samples was analyzed by X-ray diffraction (XRD) with Cu Kα radiation (model D/max RA, Rigaku Co., Japan). X-ray photoelectron spectroscopy (XPS) with Al Kα X-rays (hν = 1486.6 eV) radiation operated at 150 W (Thermo ESCALAB 250, USA) was used to investigate the surface properties. Fourier transform infrared (FT-IR) spectra were recorded on a Nicolet Nexus spectrometer on samples embedded in KBr pellets. Scanning electron microscopy (SEM, model JSM-6490, JEOL, Japan) and transmission electron microscopy (TEM, JEM-2010, Japan) were used to characterize the morphology and structure. N_2 adsorption-desorption isotherms were obtained on N_2 adsorption apparatus (ASAP 2020, Micromeritics, USA). The UV-vis diffuse-reflectance spectrometry (UV-vis DRS) spectra were obtained for the dry-pressed disk samples using a scanning UV-vis spectrophotometer (TU-1901, China) equipped with an integrating sphere assembly, using 100% $BaSO_4$ as the reflectance sample. Photoluminescence (PL) studies (F-7000, HITACHI, Japan) were conducted to investigate the optical properties of the samples. The photocurrent was measured by an electrochemical system (CHI-660B, Chenhua, China). And for the photocurrent measurement, the working electrode was irradiated by a 300 W Xe lamp with a 420 nm cut-off filter. Steady and time-resolved fluorescence emission spectra were recorded at room temperature with a fluorescence spectrophotometer (Edinburgh Instruments, FLSP-920). Electron spin resonance (ESR) of radicals spin-trapped by 5, 5-dimethyl-1-pyrroline N-oxide (DMPO) was recorded on a JES FA200 spectrometer. Samples for ESR measurement were prepared by mixing the samples in a 50 mM DMPO solution tank (aqueous dispersion for DMPO-$\bullet$OH and methanol dispersion for DMPO-$\bullet O_2^-$) and irradiated with visible-light.

2.3 Evaluation of photocatalytic activity

The photocatalytic activity was evaluated by the removal efficiency of NO at ppb levels in a continuous flow reactor with 0.2 g prepared samples. And the concentration of NO was continuously detected by a NO_x analyzer (Thermo Environmental Instruments Inc., model 42c-TL). A 150 W commercial tungsten halogen lamp was vertically placed above the reactor and the lamp turned on when the adsorption-desorption equilibrium achieved. The detailed description of photocatalytic apparatus are presented in Supporting Information.

2.4 In situ DRIFTS investigation

In situ DRIFTS measurements were conducted using the TENSOR II FT-IR spectrometer (Bruker) equipped with an in situ diffuse-reflectance cell (Harrick) and a high temperature reaction chamber (HVC), as shown in Scheme 1. The reaction chamber equipped with three gas ports and two coolant ports. High-purity He, high-purity O_2 and 100 ppm of NO (in He) mixture can be fed into the reaction system and a three-way ball valve is used to switch the target gas (NO) and purge gas (He). The total gas flow rate was 100 mL/min and the concentration of NO is 50 ppm by the dilution of O_2. The chamber is enclosed with a dome with three windows, two for IR light entrance and detection, and one for illuminating of the photocatalyst. The observation window is UV quartz and ZnSe for the other two windows. And Xe lamp (MVL-210, Optpe, Japan) was used for irradiation light source. The prepared samples were put into a vacuum tube for pretreated 1h at 300℃ before measurement.

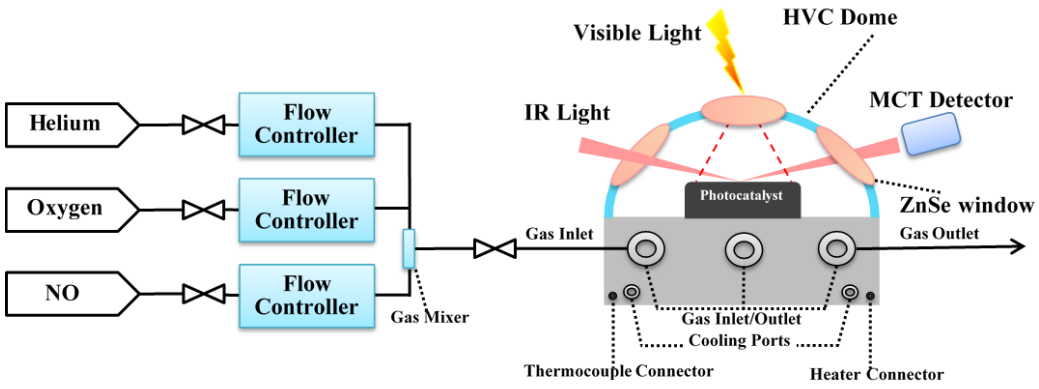

Scheme 1. The designed reaction system for the in situ DRIFTS signal recording.

2.5 DFT calculations

All the spin-polarized DFT-D2 calculations were performed by applying the code

VASP5.3.5,[30, 31] utilizing the generalized gradient approximation with the PBE exchange and correlation functional.[32] The projector-augmented wave (PAW) method was employed, with a cut-off energy of 400 eV.[33] The Brillouin zone was set using a 5 × 5 × 1 K-points. All atoms were allowed to be relaxed and converged to 0.02 eV/Å. The nudged elastic band (NEB) method [34, 35] was used to search the reaction pathways from the initial state (IS) to respective final state (FS), and the transitional state (TS) was determined with the climbing image method and verified with a single imaginary frequency (f/i).

3. RESULTS AND DISCUSSION

3.1 Chemical composition and phase structure

The chemical structure and composition of CN and SCO-ACN-0.1 are examined by XPS measurements. In XPS survey spectra (Figure S1a and S1b in Supporting Information), C1*s*, N1*s*, Sr3*d* and O1*s* signals can be observed in SCO-ACN-0.1 sample. As shown in Figure S1c, the corresponding binding energies of C1*s* at 284.6 and 288.1 eV can be ascribed to sp^2 C−C bonds and sp^2-bonded carbon in N-containing aromatic rings (N–C=N) respectively.[36, 37] The N1*s* spectra can be deconvoluted into four peaks at 398.8 eV, 400.4 eV, 401.6 eV and 404.5 eV (Figure 1a). The main peak centered at 398.8 eV originates from the sp^2-bonded N involved in the triazine rings (C–N=C), and the weak peak at 400.4 eV is due to the tertiary nitrogen N–$(C)_3$ groups in CN.[36, 37] And the C–N=C, N–$(C)_3$ and N–C=N groups make up the basic substructure units of CN polymers and then construct the heptazine heterocyclic ring (C_6N_7) units. Notably, the peak (at 401.6 eV) of amino functions (C–N–H) can obviously be observed in CN sample but its intensity is weak in SCO-ACN-0.1, indicating some of the hydrogen bonds in the intralayer framework of CN have been eliminated. Furthermore, the atomic ratio of carbon to nitrogen (C : N) gradually increases from 3 : 4.34 for the pristine CN to 3 : 3.60 for SCO-ACN-0.1 (Table S1 in Supporting Information), demonstrating that the amine groups (NH_2/NH) from CN are partially lost along with the breaking of hydrogen bonds.[20] Hence the microstructure of CN would be changed by breaking the hydrogen bonds through the reaction between CN and $SrCO_3$ in co-pyrolysis process. The related high-resolution

spectra of Sr3*d* and O1*s* are shown in Figure 1b and S1d, which indicates that strontium oxide are formed on the CN surface.

Subsequently, X-ray diffraction is employed to elucidate the crystal structures of the as-prepared samples. The formation of CN polymer is indicated by the two characteristic diffraction peaks at 13.1 ° and 27.2 °, which arise from the in-plane structural repeating motifs of the aromatic systems and the interlayer reflection of a graphite-like structure, respectively.[38, 39] As shown in Figure 1c, the two peaks of SCO-ACN-X samples gradually disappear or depressed with the increasing addition of $SrCO_3$. The disappeared peak at 13.1 ° intuitively reflects that the in-plane periodicity of the aromatic systems has been destroyed. And the formed irregular intralayer structure would induce the interlayer structure to be fluctuated and then disturb the periodic stacking of the layers. So with the introduction of $SrCO_3$, there is no characteristic diffraction peaks of CN observed in SCO-ACN-X samples. At the same time, the characteristic diffraction peaks of $SrCO_3$ have not been detected in SCO-ACN-X samples. However, the pattern of SCO-CN developed by ex-situ method displays both the characteristic diffraction peaks of $SrCO_3$ and CN. So combining the XPS results, we can conclude that the synergic interactions between CN and $SrCO_3$ during the in-situ thermal processes would break the intralayer hydrogen bonds, resulting in the formation of ACN.

In order to verify whether the basic atomic structures of CN would be destroyed via the amorphism by breaking of intralayer hydrogen bonds, the FT-IR spectra are measured (Figure 1d). The strong adsorption band of heptazine heterocyclic ring (C_6N_7) units at 1700-1200 cm^{-1} have been detected.[40] And the sharp peak at 810 cm^{-1} corresponding to the breathing mode of heptazing ring system also can be observed, which indicates that the SCO-ACN-X samples maintain the basic CN atomic structures.[41] The broad peak located at 3500-3100 cm^{-1} can be attributed to the residual N-H components and the O-H bands, associated with the uncondensed amino groups and the absorbed H_2O molecules, respectively. It is important to note that the absorption intensity of N-H components at 3500-3100 cm^{-1} decrease gradually with the addition of $SrCO_3$. Moreover, the absorption band at 890 cm^{-1} assigned to

deformation mode of N-H is gradually depressed as well. Furthermore, a newly generated absorption band at 2166 cm^{-1} can be observed in SCO-ACN-X, which is the stretching vibration mode of N=C=N. The change of the IR bands indicates that the introduction of $SrCO_3$ in the urea polymerization process only destroys the periodic arrangement of the interlayers melon strands and maintains the basic atomic structures of the strands to form the unique amorphous arrangements of short-range order but long-range disorder. Therefore, a facile co-pyrolysis method can be employed to synthesize ACN by breaking the hydrogen bonds to destroy the intralayer long-range atomic order arrangements.

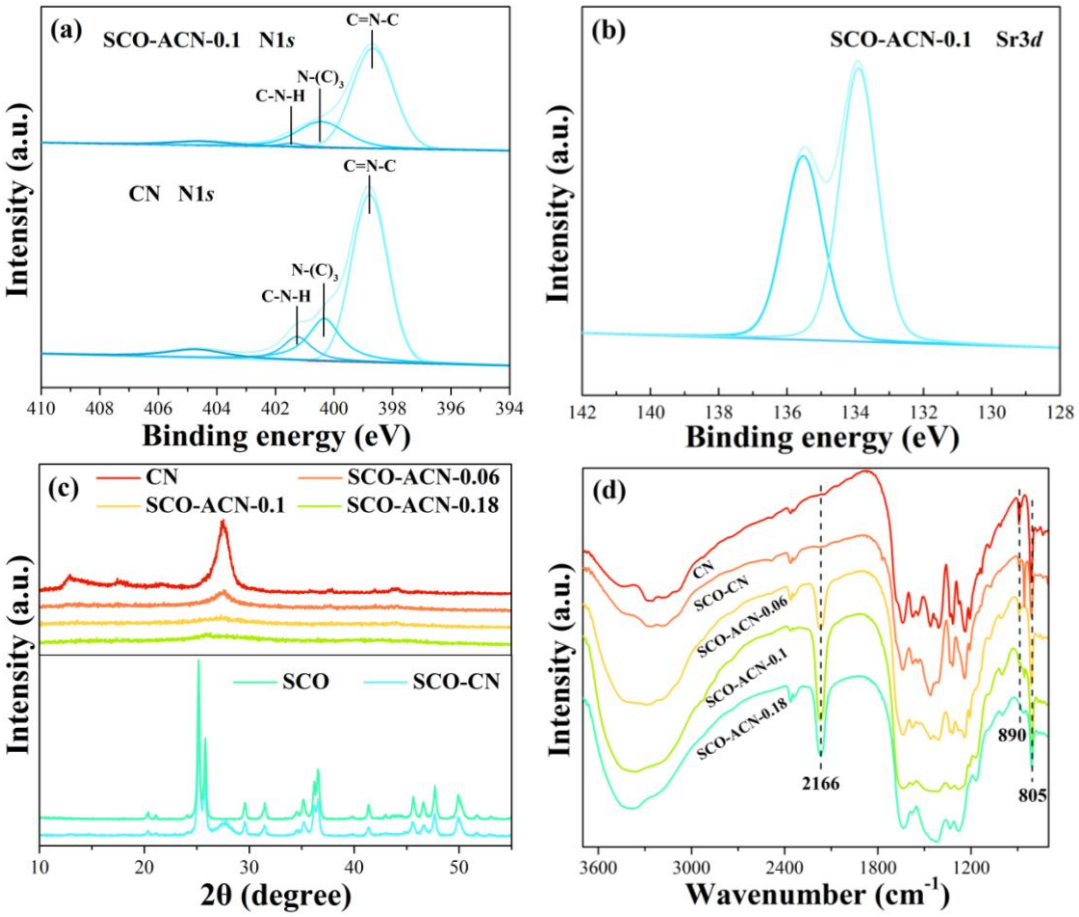

Figure 1. The N1*s* XPS spectra of CN and SCO-ACN-0.1 (a), high-resolution Sr3*d* XPS spectra of SCO-ACN-0.1 (b), XRD pattern (c) and FT-IR spectra (d) of CN and SCO-ACN-X.

3.2 Morphology and formation mechanism

The SEM images are presented to investigate the morphology differences between original CN and ACN. As shown in Figure 2a-d, the pristine CN are formed by the stack of silk-like nanosheets, and SCO-ACN-X samples generally maintain similar

morphology. Careful observation indicates that a number of pores can be clearly observed in SCO-ACN-X samples compared to the pristine CN. The formation of this special porous structure should be associated with the interaction between CN and $SrCO_3$. Concretely, during the co-pyrolysis process, the CO_3^{2-} in $SrCO_3$ will attack hydrogen bonds of CN to release H_2 and CO_2 gas probably in the form of bubbles, resulting in the breaking of the intralayer hydrogen bonds of CN and the formation of ACN. The burst of the bubbles lead to the formation of porous structure. Utilizing the DFT method, nudged elastic band (NEB) calculations are thus carried out to further confirm this deduction. As shown in Figure 2f, lower energy barrier and less energy adsorption are observed in the reaction at edge sites of CN, suggesting that CO_3^{-} is prior to attack the hydrogen bonds at edge sites, compared to that of bridge sites (Refer Figure S2 in Supporting Information for detailed descriptions of the two reaction pathways). This result indicates that the special porous structure dominantly originates from the H_2 and CO_2 gas generation at the edge sites of CN. Therefore, the increased exposure of bare edge in SCO-ACN-X is certified, which contributes to the construction of ACN. Besides, the EDX elemental mapping of SCO-ACN-0.1 shown in Figure 2e suggests that the C, N, Sr and O elements are distributed uniformly. However, what is the actual form of residual SrO?

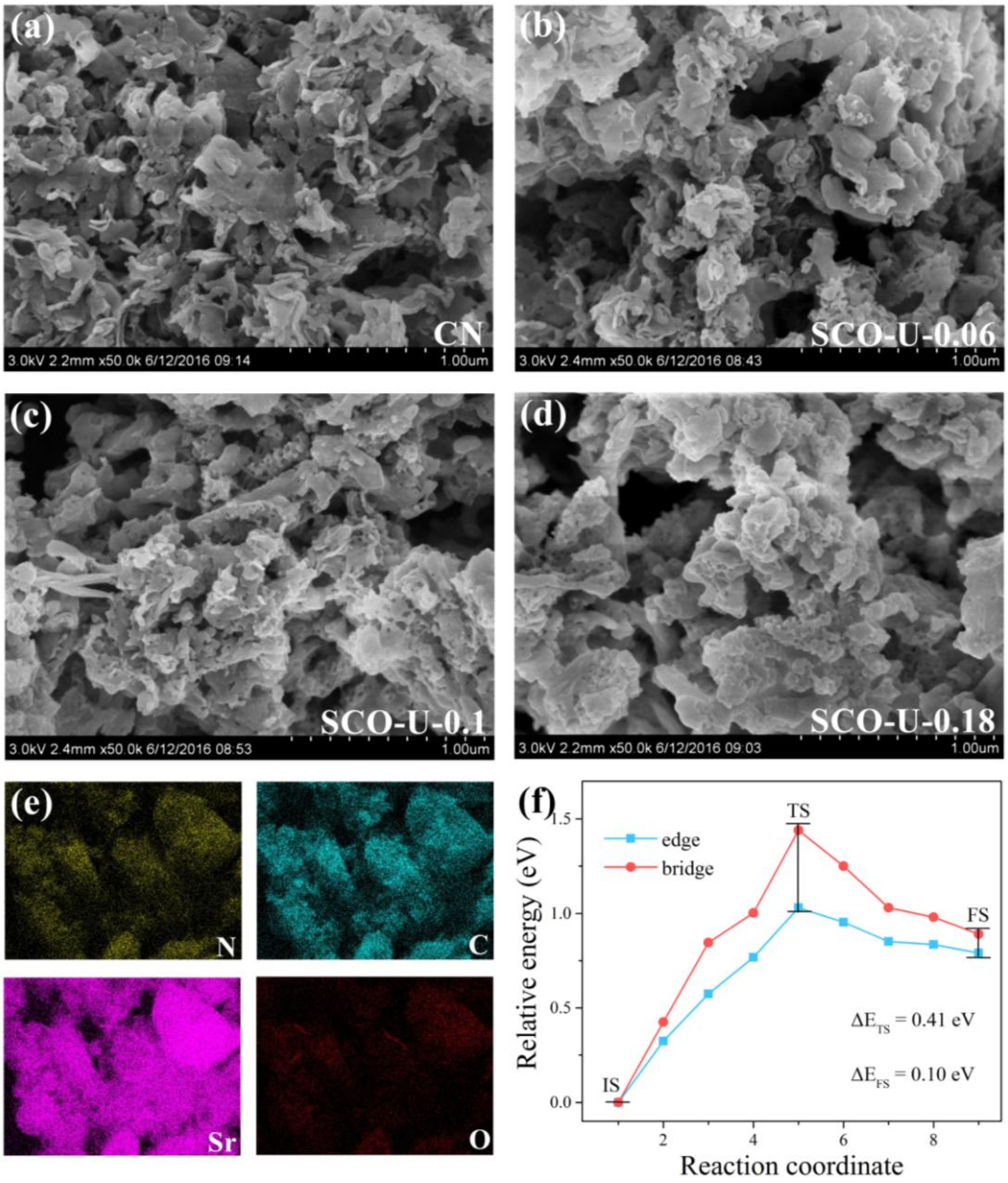

Figure 2. SEM images of as-prepared samples (a-d), EDX elemental mapping of N, C, Sr and O in image for SCO-ACN-0.1 sample (e) and relative energy comparison for $CO_3^{2-} \rightarrow HCO_3^-$ reaction at bridge and edge sites of carbon nitride (f).

Next, the TEM is further used to reveal the microstructure, as shown in Figure 3. Compared to the primary layered CN nanosheets, there are clear lattice fringes with lattice spacing of 2.581 Å can be observed (circled by red dash line) in SCO-ACN-0.1 sample, which match the spacing of the (200) crystal planes of the SrO clusters (2-5 nm) formed by the thermal decomposition of $SrCO_3$ during co-pyrolysis process. Hence a facile co-pyrolysis method has been developed to construct amorphous carbon nitride decorated with SrO clusters.

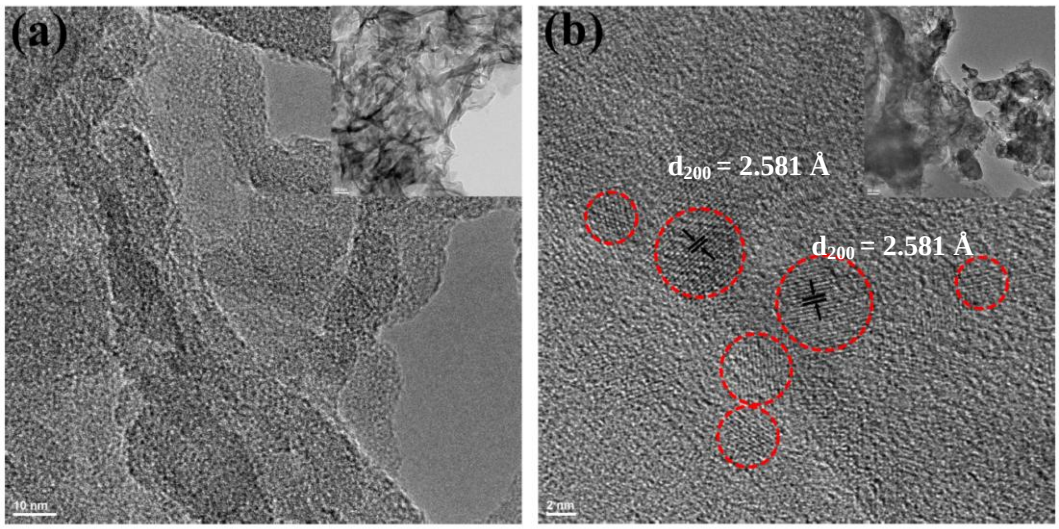

Figure 3. TEM and HRTEM images of CN (a) and SCO-ACN-0.1 (b).

In addition, the N_2 adsorption-desorption isotherms and Barrett-Joyner-Halenda (BJH) pore-size distribution curves (Figure. S3) also reflect the formation of mesopores. The specific surface area and pore volume of SCO-ACN-X are decreased and relevant parameters are listed in Table S1. And according to the comparison, the specific surface area and porous structures should not be the key factors in the enhanced photocatalytic activity for SCO-ACN-X.

3.3 Optical properties, charge separation and transfer

The PL spectra and ns-level time-resolved fluorescence decay spectra were recorded in Figure 4 to investigate the transfer of photogenerated carriers. As shown in Figure 4a, in contrast to a strong band-to-band emission peak at 442 nm for CN, SCO-ACN-0.1 sample exhibits a much depressed PL peak. The quenching of the PL peaks can be ascribed to the inhibition of radiative recombination pathways, which are associated with the unique short-range order but long-range disorder amorphous arrangements of ACN that could eliminate the high localization of charge carriers within each melon strand and decrease the large potential barrier in the regions between the layers and across the hydrogen bonds to boost the separation of charge carriers.[20, 21] The SrO has a band gap 6.1 eV with conduction band (CB) and valence band (VB) positions at -3.08 and 3.02 eV, repectively.[42, 43] Considering the band structure of carbon nitride, the visible light induced carriers from ACN could not transfer to SrO. Thus, the enhanced charge separation and transfer characteristic of

SCO-ACN is irrelevant to the SrO clusters. Correspondingly, the radiative lifetime of SCO-ACN-0.1 is longer than CN, further confirming the effective transfer of carriers to inhibit the recombination of electron-hole pairs directly originating from the special amorphous structure. Besides, the photocurrent density-time response plot via on-off cycles of samples under visible-light irradiation is employed to evaluate the interfacial charge separation dynamics (Figure S4a). Owing to the enhanced electron-hole separation and transfer, the photocurrent responding intensity of SCO-ACN-0.1 is higher than primary CN. As shown in Figure S4b, a typical semiconductor absorption in the blue light range is observed for all samples. And the addition of $SrCO_3$ in thermal treatment process could increase the visible-light utilization, induce the red-shift of optical absorption band edge and broaden the visible-light absorption region.

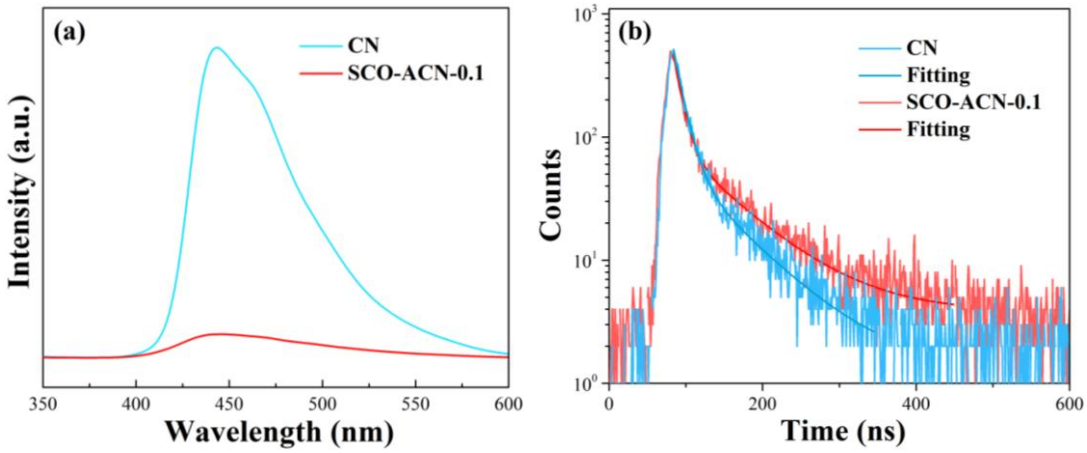

Figure 4. PL spectra (a), ns-level time-resolved fluorescence spectra (b) for as-prepared samples.

3.4 Photocatalytic activity and conversion pathway of NO oxidation

As shown in Figure 5a, all SCO-ACN-X samples exhibit a superior activity to pristine CN. Among them, SCO-ACN-0.1 sample can reach an unprecedented high NO removal ratio of 50.0%. So a facile co-pyrolysis method has been developed to construct highly efficient SCO-ACN and the optimized preparation condition is confirmed. To further demonstrate the interaction between CN and $SrCO_3$ during the co-pyrolysis process, the mechanical mixture sample SCO-CN is also tested and there is a slight enhancement of photocatalytic activity. Therefore, the combined disrupting of the intralayer long-rang atomic order structure of CN and the coupling with SrO

clusters are beneficial to enhance the photocatalytic activity.

The photocatalytic efficiency is strongly related to the number of the electron-hole pairs generated under light irradiation, as well as their evolution route. The photogenerated electrons and holes can migrate to the surface of the photocatalysts and then be trapped, generally by the oxygen and surface hydroxyls, to ultimately form superoxide radicals ($\bullet O_2^-$) and hydroxyl radicals (•OH) that react with the adsorbed pollutant. To further investigate the reactive species responsible for photocatalytic removal of NO, ESR spin-trap with DMPO technique were employed to detect the DMPO-$\bullet O_2^-$ and DMPO-•OH signals in CN and SCO-ACN-0.1 suspension (Figure 5b). As expected, a much stronger DMPO-$\bullet O_2^-$ signal was observed for SCO-ACN-0.1 than that for CN. This improvement is associated with the improved electron excitation property and the better charge transfer characteristic which facilitate the generation of photogenerated electrons to trap the molecular oxygen and produce more $\bullet O_2^-$. Interestingly, a strong DMPO-•OH adduct signal generated by SCO-ACN-0.1 is detected. The potential energy of valence band (VB) holes (1.40 eV) from CN are more negative than the OH^-/•OH and H_2O/•OH potentials (1.99 and 2.37 eV) and cannot directly oxidize OH^-/H_2O into •OH radicals. However, the observed •OH radicals in Figure 5b can be formed through the reduction of $\bullet O_2^-$ via a route of $\bullet O_2^- \rightarrow H_2O_2 \rightarrow$ •OH. Therefore, we conclude that the SCO-ACN could significantly promote transportation, migration and transformation of charge carriers and then facilitate the generation of reactive radicals for NO oxidation.

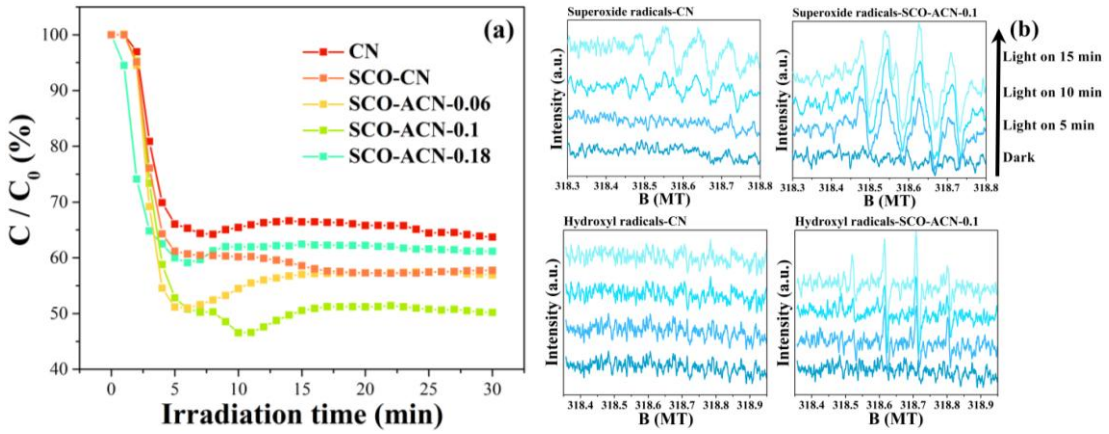

Figure 5. Visible-light photocatalytic activities of as-prepared samples for NO removal (a), and DMPO spin-trapping ESR spectra of samples (b).

To understand the photocatalytic NO oxidation mechanism, *in situ* DRIFTS were carried out to track the time-dependent evolution of reaction intermediates and products over the photocatalysts surface, as shown in Figure 6. The background spectrum is recorded before injecting NO into the reaction chamber. The NO absorption bands appear once the NO contacts the photocatalyst at 25 ^{o}C in dark condition. On the surface of CN, the absorption bands of N_2O at 2282 and 2244 cm^{-1} have been detected, indicating the adsorption of NO over CN.[24, 25] In OH stretching region, a negative band at around 3550 cm^{-1} is observed and the adsorption IR bands at 1193-1142 cm^{-1} of NO^{-}/NOH and at 2087 and 934 cm^{-1} of NO_2 have also been detected. This result indicates the disproportionation of NO on the surface of CN. The following reaction can be proposed: $3NO + OH^{-} = NO_2 + NO^{-} + NOH$.[24-27] And the other absorption bands developed progressively can be assigned to the stretching vibration of monodentate (at 1060-1010 cm^{-1}), bidentate (at 1125 and 1109 cm^{-1}) nitrites or bidentates (at 1227 and 1060-1010 cm^{-1}), bridging (at 1001cm^{-1}), chelating bidentate (at 986 cm^{-1}) nitrates.[24-26, 28, 29, 44] The formation of nitrites and nitrates over CN during the NO adsorption process are mainly due to the active pyridine nitrogen sites embedded inside the carbon matrix that facilitate the formation of the activated oxygen species and then enhance the oxidation capacity of surface oxygen species for NO_x oxidation.[45, 46]

In the case of SCO-ACN-0.1, nitro compounds adsorption can be observed before the visible-light irradiation, as shown in Figure 6c, similar to that of NO adsorption over CN sample. However, significant differences can be identified. An outstanding band associated with nitrosyl (Sr-$NO^{\delta(+)}$) appears at 2126 cm^{-1}, which is the reaction intermediate of NO oxidation.[47, 48] NO molecules are inclined to form nitrosyl, which is associated with the interaction with SrO to form more stable reaction intermediate (nitrosyls).[27, 48] The nitrosyl was formed by partial charge transfer from the 5s orbital of NO to Sr^{2+} to form Sr-$NO^{\delta(+)}$.[25, 48] This is consistent with the observation that the vibration frequencies of nitrosyls are higher than those of NO molecules (1876 cm^{-1})

but lower than those of NO^+ free ions (around 2200 cm^{-1}). The adsorbed nitrosyls as the main reaction intermediates would be preferentially oxidized to nitro compounds by reactive oxygen species.[48] Hence SrO clusters can be identified as the newly formed active centers to facilitate the activation of NO via the formation of Sr-$NO^{\delta(+)}$, which could effectively promote the conversion of NO to final products.

With the adsorption equilibrium being achieved, a visible-light source is applied to initiate the photocatalysis reaction. Figure 6b shows the IR spectra for CN under visible-light irradiation in time sequence. The spectrum of "base line" is the same with that of "NO + O_2 20 min" in Figure 6a. In the range of 2300-2050 cm^{-1}, the absorption bands at 2282 and 2244 cm^{-1} disappear, indicating the consumption of N_2O/NO accumulated in NO adsorption process. Correspondingly, the peaks intensity of some intermediates (nitrito, NO^-/NOH) and final products (nitrites, nitrates) are significantly increased. The ESR results demonstrated that the surface superoxide radicals are the major radical species (Figure 5b). Thus the superoxide radicals should be responsible for the conversion of intermediates into final products under visible-light irradiation. The adsorption-photocatalysis mechanism is illustrated in Scheme 2a.

The time-dependent IR spectra of photocatalytic NO oxidation over SCO-ACN-0.1 are recorded and shown in Figure 6d. In the range of 1250-900cm^{-1}, the tendency of IR absorption bands is similar to CN. The increased negative peak intensity of OH groups at 3700-3350 cm^{-1} can attribute to the consumption of OH groups for the generation of hydroxyl radicals, which is one of the oxidation mediators for NO removal. A slightly intensified band of Sr-$NO^{\delta(+)}$ at 2126 cm^{-1} can be observed. And it is noteworthy that a new absorption band at 2215 cm^{-1} can be detected, which can be ascribed to the fact that electrons of adsorbed NO are trapped by the photogenerated hole and then convert into NO^+ (free ions). And the formed Sr-$NO^{\delta(+)}$ and NO^+ are the dominated products for NO activation on SCO-ACN. The conversion pathway of NO adsorption and photocatalytic NO oxidation processes on SCO-CAN are proposed for the first time as depicted in Scheme 2b.

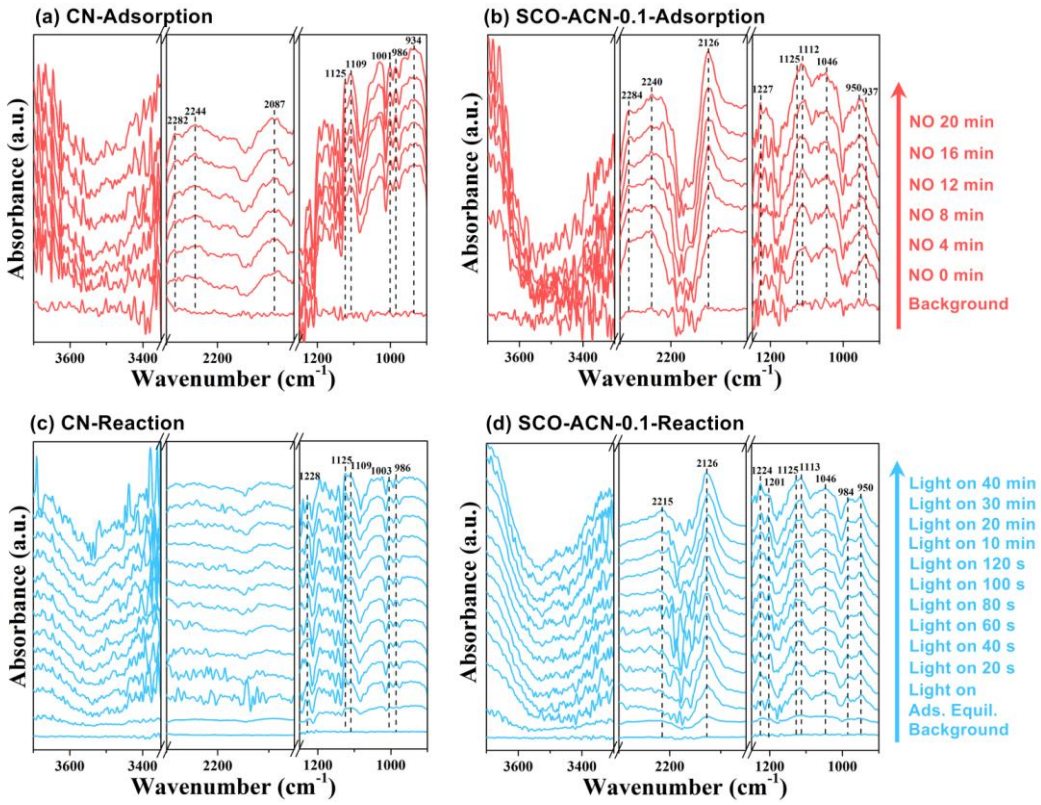

Figure 6. In situ IR spectra of NO adsorption and visible-light reaction processes over CN and SCO-ACN-0.1.

According to the comparison of adsorption and photocatalysis processes between CN and SCO-ACN-0.1, some differences can be found. Firstly, owing to the introduction of $SrCO_3$, the NO molecules tend to be adsorbed on SrO clusters to form Sr-$NO^{\delta(+)}$, and this reaction intermediates would be preferentially oxidized by reactive oxygen species. Secondly, the increased consumption of OH groups in SCO-U-0.1 during the reaction process is not only beneficial to the conversion of intermediates but also contributes to the generation of hydroxyl radicals, in accordance with the ESR results. Last but not least, although the adsorption process and photocatalytic NO oxidation reactions with SCO-ACN demonstrate a bit difference from pristine CN, the SrO clusters do not change the overall conversion pathway of photocatalytic NO oxidation. Significantly, the SrO clusters as newly formed active center facilitate the activation of NO via the formation of Sr-$NO^{\delta(+)}$/NO^+ and promote the conversion of NO to final products (Scheme 2c). Therefore, both the conversion pathway of photocatalytic NO oxidation and the reasons for enhanced photocatalytic activity can

be directly reflected by in situ DRIFTS.

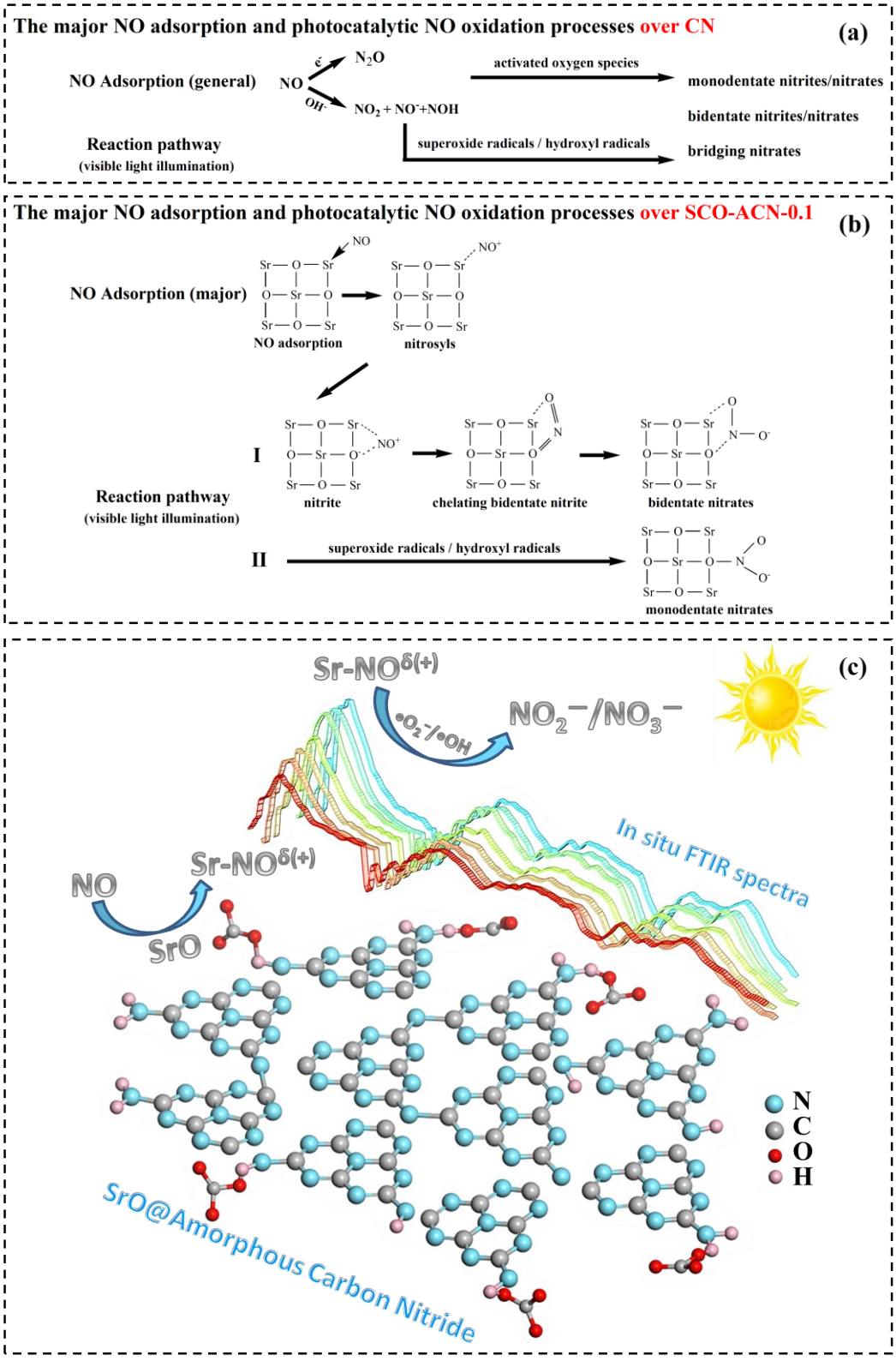

Scheme 2. The conversion pathways of adsorption and photocatalytic oxidation of NO over CN (a) and SCO-ACN-0.1 (b), the illustration of the catalyst structure and key role of SrO clusters (c).

In summary, a facile co-pyrolysis method was developed to construct

SrO@amorphous carbon nitride for efficient NO removal. The SCO-ACN exhibited substantially enhanced visible-light photocatalytic NO removal ascribing to the promoted transportation, migration and transformation of charge carriers benefited from the amorphous property of ACN and the enhanced activation of NO via the formation of Sr-$NO^{\delta(+)}$. The time-dependent *in situ* IR spectra revealed the evolution of intermediates during NO adsorption and photocatalytic NO oxidation processes. The differences of adsorption and photocatalysis reaction between pristine CN and SCO-CAN were compared. And the SrO clusters did not change the general conversion pathway of photocatalytic NO oxidation of CN. Instead, the SrO clusters were identified as newly formed active centers to promote the conversion of NO into final products. The present work could provide a facile method to construct highly efficient amorphous carbon nitride and offer new strategy to the understanding of conversion pathway in gas-phase photocatalytic reaction.

ASSOCIATED CONTENT

Supporting Information.

Evaluation of photocatalytic activity. The XPS survey spectra of CN (a) and SCO-ACN-0.1 (b), high-resolution C1*s* (c) and O1*s* (b) XPS spectra of SCO-U-0.1 sample. Optimized structures of pristine g-C_3N_4, CO_3^{2-} and HCO_3^- ions (a). Reactions pathways of HCO_3^- generation at edge (b) and bridge (c) sites in CN. N_2 adsorption-desorption isotherms curves (a) and pore-size distribution (b) of as-prepared samples. Table about S_{BET}, pore volume, formula and NO removal ratio of samples. Transient photocurrent densities (a) and UV-vis DRS spectra (b) for as-prepared samples. Table about assignments of the FT-IR bands observed during NO adsorption over photocatalysts. Table assignments of the FT-IR bands observed during photocatalytic NO oxidation processes over photocatalysts. These materials are available free of charge via the Internet at http://pubs.acs.org.

ACKNOWLEDGMENTS

This research was financially supported by National Natural Science Foundation of China (51478070, 21501016 and 51108487), the National Key R&D project

(2016YFC0204702), and the Innovative Research Team of Chongqing (CXTDG201602014).

Author Contributions

The manuscript was written through contributions of all authors. All authors have given approval to the final version of the manuscript.

REFERENCES

(1) Brauer, M.; Amann, M.; Burnett, R. T.; Cohen, A.; Dentener, F.; Ezzati, M.; Henderson, S. B.; Krzyzanowski, M.; Martin, R. V.; Dingenen, R. V.; Donkelaar A. V.; Thurston G. D., Exposure assessment for estimation of the global burden of disease attributable to outdoor air pollution. *Environ. Sci. Technol.* **2012,** *46* (2), 652-660.

(2) Brauer, M.; Freedman, G.; Frostad, J.; Van, D. A.; Martin, R. V.; Dentener, F.; Van, D. R.; Estep, K.; Amini, H.; Apte, J. S., Ambient air pollution exposure estimation for the global burden of disease 2013. *Environ. Sci. Technol.* **2015,** *50* (1), 79-88.

(3) West, J. J.; Cohen, A.; Dentener, F.; Brunekreef, B.; Zhu, T.; Armstrong, B.; Bell, M. L.; Brauer, M.; Carmichael, G.; Costa, D. L.; Dockery, D. W.; Kleeman, M.; Krzyzanowski, M.; Künzli, N.; Liousse, C.; Lung, S. C. C.; Martin, R. V, Pöschl, U., Pope, C. A.; Roberts, J. M.; Russell, A. G.; Wiedinmyer, C., What we breathe impacts our health: improving understanding of the link between air pollution and health. *Environ. Sci. Technol.* **2016**, *50*, 4895-904.

(4) Ma, J. Z.; Wu, H. M.; Liu, Y. C.; He, H., Photocatalytic removal of NO_X over visible light responsive oxygen-deficient TiO_2. *J. Phys. Chem. : C.* **2014,** *118* (14), 7434-7441.

(5) Dong, F.; Wang, Z. Y.; Li, Y. H.; Ho, W. K.; Lee, S. C., Immobilization of polymeric g-C_3N_4 on structured ceramic foam for efficient visible light photocatalytic air purification with real indoor illumination. *Environ. Sci. Technol.* **2014,** *48* (17), 10345-10353.

(6) Heo, I.; Kim, M. K.; Sung, S.; Nam, I. S.; Cho, B. K.; Olson, K. L.; Li, W., Combination of photocatalysis and HC/SCR for improved activity and durability of DeNOx catalysts. *Environ. Sci. Technol.* **2013,** *47* (8), 3657-64.

(7) Guo, Q. B.; Sun, T. H; Wang, Y. L.; He, Y.; Jia, J. P., Spray absorption and electrochemical reduction of nitrogen oxides from flue gas. *Environ. Sci. Technol.* **2013,** *47* (16), 9514-22.

(9) Tong, H.; Ouyang, S. X.; Bi, Y. P.; Umezawa, N.; Oshikiri, M.; Ye, J. H., Nano-photocatalytic materials: possibilities and challenges. *Adv. Mater.* **2012,** *24* (2), 229-51.

(10) Ai, Z. H.; Ho, W. K.; Lee, S. C.; Zhang, L. Z., Efficient photocatalytic removal of NO in indoor air with hierarchical bismuth oxybromide nanoplate microspheres under visible light. *Environ. Sci. Technol.* **2009,** *43* (11), 4143-50.

(11) Wang, X. C.; Maeda, K.; Thomas, A.; Takanabe, K.; Xin, G.; Carlsson, J. M.; Domen, K.; Antonietti, M. A metal-free polymeric photocatalyst for hydrogen production from water under visible light. *Nat. Mater.* 2009, *8* (1), 76-80.

(12) Ong, W. J.; Tan, L. L.; Ng, Y. H.; Yong, S. T.; Chai, S. P., Graphitic carbon nitride ($g\text{-}C_3N_4$)-based photocatalysts for artificial photosynthesis and environmental remediation: are we a step closer to achieving sustainability? *Chem. Rev.* **2016,** *116* (12), 7159.
(13) Wang, X. C.; Blechert, S.; Antonietti, M., Polymeric graphitic carbon nitride for heterogeneous photocatalysis. *ACS Catal.* **2012,** *2* (8), 1596–1606.
(14) Jiang, G. M.; Li, X. W.; Lan, M. N.; Shen, T.; Lv, X. S.; Dong, F.; Zhang, S., Monodisperse bismuth nanoparticles decorated graphitic carbonnitride: Enhanced visible-light-response photocatalytic NO removaland reaction pathway. *Appl. Catal. B : Environ.* **2017**, *205*, 532-540.
(15) Yan, H. J., Soft-templating synthesis of mesoporous graphitic carbon nitride with enhanced photocatalytic H_2 evolution under visible light. *Chem. Commun.* **2012,** *48* (28), 3430-3432.
(16) Talapaneni, S. N.; Mane, G. P.; Mano, A.; Anand, C.; Dhawale, D. S.; Mori, T.; Vinu, A., Synthesis of nitrogen-rich mesoporous carbon nitride with tunable pores, band gaps and nitrogen content from a single aminoguanidine precursor. *Chemsuschem* **2012,** *5* (4), 700-708.
(17) Dong, G. H.; Zhao, K.; Zhang, L. Z., Carbon self-doping induced high electronic conductivity and photoreactivity of $g\text{-}C_3N_4$. *Chem. Commun.* **2012,** *48* (49), 6178.
(18) Ho, W. K; Zhang, Z. Z.; Wei, L.; Huang, S. P.; Zhang, X. W.; Wang, X. X.; Yu, H., Copolymerization with 2,4,6-triaminopyrimidine for the rolling-up the layer structure, tunable electronic properties, and photocatalysis of $g\text{-}C_3N_4$. *ACS Appl. Mater. Interfaces* **2015,** *7* (9), 5497-5505.
(19) Dong, F.; Zhao, Z. W.; Sun, Y. J.; Zhang, Y. X.; Yan, S.; Wu, Z. B., An advanced semimetal-organic Bi spheres-$g\text{-}C_3N_4$ nanohybrid with SPR-enhanced visible-light photocatalytic performance for NO purification. *Environ. Sci. Technol.* **2015,** *49* (20), 12432-40..
(20) Kang, Y. Y.; Yang, Y. Q.; Yin, L. C.; Kang, X. D.; Liu, G.; Cheng, H. M., An amorphous carbon nitride photocatalyst with greatly extended visible-light-responsive range for photocatalytic hydrogen generation. *Adv. Mater.* **2015,** *27* (31), 4572-4577.
(21) Kang, Y. Y.; Yang, Y. Q.; Yin, L. C.; Kang, X. D.; Wang, L. Z.; Liu, G.; Cheng, H. M., Selective breaking of hydrogen bonds of layered carbon nitride for visible light photocatalysis. *Adv. Mater.* **2016,** *28* (30), 6471-6477.
(22) Li, G.; Zhang, D.; Yu, J. C.; Leung, M. K., An efficient bismuth tungstate visible-light-driven photocatalyst for breaking down nitric oxide. *Environ. Sci. Technol.* **2010,** *44* (11), 4276-4281.
(23) Ge, S. X.; Zhang, L. Z., Efficient visible light driven photocatalytic removal of RhB and NO with low temperature synthesized $In(OH)_xS_y$ hollow nanocubes: a comparative study. *Environ. Sci. Technol.* **2011,** *45* (7), 3027-33.
(24) Hadjiivanov, K. I.; Avreyska, V.; Klissurski, D.; Marinova, T., Surface species formed after NO adsorption and NO + O_2 coadsorption on ZrO_2 and sulfated ZrO_2: an FTIR spectroscopic study. *Langmuir* **2002,** *18* (5), 1619-1625.
(25) Wu, J. C. S.; Cheng, Y. T., In situ FTIR study of photocatalytic NO reaction on photocatalysts under UV irradiation. *J. Catal.* **2006,** *237* (2), 393-404.

(26) Kantcheva, M., Identification, stability, and reactivity of NO_X species adsorbed on titania-supported manganese catalysts. *J. Catal.* **2001,** *204* (2), 479-494.
(27) Hadjiivanov, K. I., Identification of neutral and charged N_XO_Y surface species by IR spectroscopy. *Catal. Rev.* **2007,** *42* (1-2), 71-144.
(28) Zhou, Y.; Zhao, Z. Y.; Wang, F.; Cao, K.; Doronkin, D. E.; Dong, F.; Grunwaldt, J. D., Facile synthesis of surface N-doped $Bi_2O_2CO_3$: origin of visible light photocatalytic activity and in situ DRIFTS studies. *J. Hazard. Mater.* **2016,** *307*, 163-172.
(29) Kantcheva, M.; Vakkasoglu, A. S., Cobalt supported on zirconia and sulfated zirconia I.: FT-IR spectroscopic characterization of the NO_X species formed upon NO adsorption and NO/O_2 coadsorption. *J. Catal.* **2004,** *223* (2), 352-363.
(30) Kresse, G.; Furthmüller, J., Efficient iterative schemes for ab initio total-energy calculations using a plane-wave basis set. *Phys. Rev. B* **1996,** *54* (16), 11169-11186.
(31) Kresse, G.; Furthmüller, J., Efficiency of ab-initio total energy calculations for metals and semiconductors using a plane-wave basis set. *Comp. Mater. Sci.* **1996,** *6* (1), 15-50.
(32) Perdew, J. P.; Burke, K.; Ernzerhof, M., Erratum: Generalized Gradient Approximation Made Simple. *Phys. Rev. Lett.* **1996,** *77* (18), 3865-3868.
(33) Blochl, P., Projected augmented-wave method. *Phys. Rev. B* **1994,** *50* (24), 17953-17979.
(34) Henkelman, G.; Jónsson H., Improved tangent estimate in the nudged elastic band method for finding minimum energy paths and saddle points. *J. Chem. Phys.* **2000,** *113* (113), 9978-9985.
(35) Henkelman, G., A climbing image nudged elastic band method for finding saddle points and minimum energy paths. *J. Chem. Phys.* **2000,** *113* (22), 9901-9904.
(36) Thomas, A.; Fischer, A.; Goettmann, F.; Antonietti, M.; Mueller, J. O.; Schloegl, R.; Carlsson, J. M., ChemInform abstract: graphitic carbon nitride materials: variation of structure and morphology and their use as metal-free catalysts. *J. Mater. Chem.* **2008,** *40* (9), 4893-4908.
(37) Zhang, G. Q.; Zhang, J. S.; Zhang, M. W.; Wang, X. C., Polycondensation of thiourea into carbon nitride semiconductors as visible light photocatalysts. *J. Mater. Chem.* **2012,** *22* (16), 8083-8091.
(38) Fina, F.; Callear, S. K.; Carins, G. M.; Irvine, J. T. S., Structural investigation of graphitic carbon nitride via XRD and neutron diffraction. *Chem. Mater.* **2015,** *27* (7), 2612-2618.
(39) Dong, F.; Sun, Y. J.; Wu, L. W.; Fu, M.; Wu, Z. B., Facile transformation of low cost thiourea into nitrogen-rich graphitic carbon nitride nanocatalyst with high visible light photocatalytic performance. *Catal. Sci. Technol.* **2012,** *2* (7), 1332-1335.
(40) Lotsch, B. V.; Döblinger, M.; Sehnert, J.; Seyfarth, L.; Senker, J.; Oeckler, O.; Schnick, W., Unmasking melon by a complementary approach employing electron diffraction, solid-state NMR spectroscopy, and theoretical calculations-structural characterization of a carbon nitride polymer. *Chem. Eur. J.* **2007,** *13* (17), 4969-4980.
(41) Zhang, J. S.; Zhang, G. Q.; Chen, X. F.; Lin, S.; Möhlmann, L.; Dołęga, G.; Lipner, G.; Antonietti, M.; Blechert, S.; Wang, X. C., Co-monomer control of carbon

nitride semiconductors to optimize hydrogen evolution with visible light. *Angew. Chem. Int. Ed.* **2012,** *124* (13), 3237-3241.
(42) Nemade, K. R.; Waghuley, S. A., Uv-vis spectroscopic study of one pot synthesized strontium oxide quantum dots. *Results Phys.* **2013,** *3*, 52-54.
(43) Chambers, S. A.; Droubay, T.; Kaspar, T. C.; Gutowski, M., Experimental determination of valence band maxima for srtio3,tio2, and sro and the associated valence band offsets with si(001). *J. Vac. Sci. Technol. B* **2004,** *22* (4), 2205-2215.
(44) Ramis, G.; Busca, G.; Lorenzelli, V.; Forzatti, P., Fourier transform infrared study of the adsorption and coadsorption of nitric oxide, nitrogen dioxide and ammonia on TiO_2 anatase. *Appl. Catal.* **1990,** *64*, 243-257.
(45) Lin, Y. M.; Su, D. S., Fabrication of nitrogen-modified annealed nanodiamond with improved catalytic activity. *ACS Nano* **2014,** *8* (8), 7823-33.
(46) Li, J. Y.; Liu, J.; Yin, S.; Liu, Y. Q; Li, J. J.; Cen, W. L.; Chu, Y. H., Promoting mechanism of pyridine N doped carbocatalyst for SO_2 oxidation. *RSC Adv.* **2016,** *6* (89), 86316-86323.
(47) Weingand, T.; Kuba, S.; Hadjiivanov, K.; Knözinger, H., Nature and reactivity of the surface species formed after NO adsorption and NO + O_2 coadsorption on a WO_3-ZrO_2 catalyst. *J. Catal.* **2002,** *209* (2), 539-546.
(48) Zhong, L.; Yu, Y.; Cai, W.; Geng, X. X.; Zhong, Q., Structure-activity relationship of Cr/Ti-PILC catalysts using a pre-modification method for NO oxidation and their surface species study. *Phys. Chem. Chem. Phys.* **2015,** *17* (22), 15036-15045.